Nano Research

Open Access

Research Article

Asymmetric Zn–N_4–S configuration via second-shell sulfur doping for ultralow-polarization aqueous zinc–sulfur batteries

Zuoshu Wang[1], Xueyan Yang[1], Guochao Zhao[1], Dewei Wang[1]✉, and Yuhong Chen[2]

[1] *College of Materials Science and Engineering, North Minzu University, Yinchuan 750021, China*
[2] *Ningxia Key Laboratory of Powder Materials Intelligent Design and Manufacturing, North Minzu University, Yinchuan 750021, China*

Cite this article: *Nano Research*, **2026**, *19*, 94908560. https://doi.org/10.26599/NR.2026.94908560

ABSTRACT: The development of aqueous zinc–sulfur batteries (AZSBs) is primarily plagued by the sluggish kinetics and poor reversibility of the solid–solid sulfur conversion reaction. Herein, we report a Zn single-atom catalyst embedded within a N, S-doped porous carbon matrix (Zn SAs/NSC) as an efficient sulfur host to tackle these challenges. A one-step pyrolysis of zeolitic imidazolate frameworks (ZIFs) with potassium thiosulfate ($K_2S_2O_3$) was employed to produce hierarchical pore structure with large specific surface area of 2135.5 $m^2 \cdot g^{-1}$ and incorporation of sulfur atoms in the second coordination shell of Zn–N_4 sites, resulting in an asymmetric Zn–N_4–S configuration. When employed as a sulfur host, the Zn SAs/NSC-800-based cathode delivers a notable discharge capacity of 1610.6 $mAh \cdot g^{-1}$ at 0.1 $A \cdot g^{-1}$ with an ultralow polarization voltage of 0.276 V. It also exhibits good rate capability (1229.1 $mAh \cdot g^{-1}$ at 5 $A \cdot g^{-1}$) and long-term cycling stability (60% capacity retention after 1000 cycles). Density functional theory (DFT) calculations reveal that the Zn–N_4–S sites can enhance the adsorption energy of ZnS (−2.08 eV) and facilitate electron transfer, thereby reducing the energy barrier for the solid–solid conversion. This work demonstrates the significant roles of metal single-atom coordination microenvironment in enhancing the electrochemical performance of AZSBs.

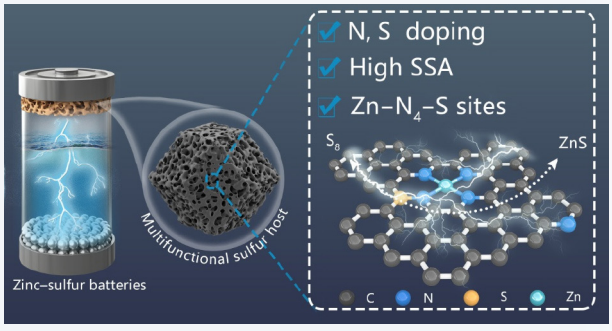

KEYWORDS: aqueous zinc–sulfur batteries, metal single-atom, porous carbon, coordination environment, electrocatalyst

1 Introduction

The energy crisis and environmental degradation increased the demand for efficient, safe, and sustainable energy storage devices [1, 2]. Aqueous-based batteries present fascinating substitutes for lithium-ion batteries thanks to their non-flammable, environmentally benign, and cost-effective [3, 4]. Aqueous zinc-ion batteries (AZIBs) have emerged as a promising candidate benefiting from the unique features of zinc metal anode. The high theoretical capacity (820 $mAh \cdot g^{-1}$) with a low redox potential (−0.76 V vs. standard hydrogen electrode (SHE)), as well as its natural abundance, make zinc metal anode very suitable for scalable energy storage [5–9]. Sulfur cathodes, which can offer an ultra-high theoretical capacity of 1675 $mAh \cdot g^{-1}$ along with natural abundance and environmental friendliness, represent a scalable solution for aqueous zinc–sulfur batteries (AZSBs) [10, 11]. Totally different from the polysulfide dissolution and shuttling in organic lithium–sulfur batteries, AZSBs display a direct solid–solid conversion from S to ZnS [12, 13], which affords an extended cycle life. Nevertheless, the solid–solid conversion mechanism still presents several challenges. The sluggish solid–solid conversion kinetics led to high polarization, poor rate performance, and limited sulfur utilization [14–16]. In addition, both sulfur and zinc sulfide (ZnS) are almost insulators, which severely hinders charge transfer [11, 17, 18]. Besides, the substantial volume expansion (~ 53%) will generate significant mechanical stress that can lead to structural degradation and loss of electrical contact, which exerts high interfacial resistance to further deteriorate the reaction kinetics [19, 20].

To address these issues, two distinct strategies have been developed. One solution is to encapsulate sulfur within carbonaceous materials (e.g., activated carbon, conductive carbon black, and carbon nanotubes) to enhance electrical conductivity. The other approach focuses on modifying the sulfur through chalcogen doping as well as introducing organic/inorganic additives into electrolyte to lower the ZnS decomposition energy

Received: December 5, 2025; **Revised:** February 8, 2026
Accepted: February 11, 2026

✉Address correspondence to wangdewei@yeah.net

barrier [13, 16, 20, 21–28]. Despite these efforts, conventional porous carbon hosts often suffer from limited specific surface area and pore volume, which lead to inadequate sulfur confinement as well as insufficient buffering of volume changes [29–31]. Moreover, the direct conversion between sulfur and ZnS involves a high energy barrier, resulting in slow reaction kinetics and considerable overpotential [31–33]. Moreover, the inherent nonpolar nature of carbonaceous materials lacks catalytic active sites to boost the reaction kinetics, which induces rapid capacity fading of the resulting AZSBs [34–36]. Although the various chemical modifications have been exploited, most strategies primarily focus on lowering the ZnS decomposition barrier [35]. It is therefore essential to develop alternative strategies that not only lower the energy barrier for solid–solid conversion but also facilitate sulfur reduction and ZnS decomposition.

Very recently, metal single atom anchored carbon matrix has emerged as an ideal sulfur host for AZSBs due to their atomically dispersed active sites and high conductivity [35–37]. Confining sulfur within the porous carbon framework can enable catalytic reactions at metal single atom sites and enhance charge transfer, which effectively mitigates insulating properties of sulfur and sluggish kinetics. For instance, Zhang et al. developed an atomically dispersed Fe site with Fe–N_4 coordination as catalytic center in the sulfur cathode [35], which delivered a high discharge capacity of 1143 mAh·g^{-1} with a low polarization voltage of 0.61 V. Moreover, it exhibited cycling stability over 300 cycles with a capacity decay rate of 0.141% per cycle. Zhang and co-workers reported the incorporation of single-atom cobalt (SA-Co) into biomass-derived porous carbon matrix as an efficient sulfur host for AZSBs [36], which delivers a high specific capacity of 1445.38 mAh·g^{-1} at 1 A·g^{-1} with a polarization voltage of 0.97 V. It also maintained 729.96 mAh·g^{-1} after 500 cycles at 4 A·g^{-1}. Dai et al. demonstrated the constructing single-atom iron catalysts (Fe-SAs) anchored on nitrogen doped carbon (Fe-NC) [37], which displayed an exceptional specific capacity of 1399 mAh·g^{-1} at a high current density of 5 A·g^{-1}, while exhibiting a low voltage hysteresis of 0.81 V. Furthermore, it showed 56% of its initial capacity after 300 cycles at 5 A·g^{-1}, indicating excellent cycling performance. Despite this progress, metal single atom anchored carbon matrix, typically in the form of nonpolar M–N_4 configurations, still exhibits limited catalytic activity. Recent studies indicate that the selectivity and electrochemical activity of single-atom catalysts are largely determined by the electronic structure of the metal center [38]. In conventional symmetric M–N_4 coordination, the uniform electron cloud distribution leads to weak polarization ability toward S–S/Zn–S bonds, making it difficult to effectively lower the bond-breaking energy barrier. Furthermore, the low specific surface area and insufficient porosity of these metal single atom anchored carbon matrices hinder buffering of volume expansion that causes structural collapse during cycling. In light of this, recent studies have demonstrated that introducing heteroatoms with different electronegativities (e.g., P, S, and B) can break the symmetry of M–N_4 and thus modulate the electronic structure of the central metal atom [39]. In particular, introducing sulfur atoms into the second coordination shell has been shown to enable electronic tuning of classical M–N_4 sites owing to its unique electron-donating properties and spatial effects [40]. This strategy effectively disrupts the electronic symmetry without altering the primary coordination structure, opening a novel pathway for optimizing the activity of metal single atoms. However, this electronic structure regulation strategy remains unexplored in AZSBs. Sulfur atoms, with their distinct electronegativity and electron-donating capabilities, can effectively modify the affinity of metal centers for sulfur-containing intermediates. Hence, there is an urgent need to design novel active sites with high polarity and strong adsorption capacity by tailoring the coordination environment of single atoms to overcome the limitations of current sulfur hosts.

To address the aforementioned challenges, we report herein the design of zinc single atom decorated within nitrogen, sulfur-doped porous carbon (Zn SAs/NSC) as a sulfur host for AZSBs. This work involves breaking the symmetry of conventional Zn–N_4 configurations through second shell sulfur doping. Specifically, we employed zeolitic imidazolate framework (ZIF) as a precursor and potassium thiosulfate ($K_2S_2O_3$) as a multifunctional activating agent for the synthesis of Zn SAs/NSC. The $K_2S_2O_3$ not only acts as a chemical activator to generate abundant micropores and mesopores but also simultaneously offers sulfur species for sulfur doping within carbon lattice during decomposition. Crucially, partial sulfur atoms were precisely positioned in the second coordination sphere through N–S bond formation, thereby successfully modifying the electronic symmetry of Zn–N_4 active sites. The resulting Zn–N_4–S sites can strengthen sulfur adsorption and boost the solid–solid conversion kinetics. Furthermore, the large surface area and pore volume of the resulting Zn SAs/NSC, combined with the high dispersion of Zn–N_4–S sites, can effectively accommodate volume expansion during cycling. Consequently, the resulting Zn SAs/NSC-based cathode achieves a large discharge capacity of 1610.6 mAh·g^{-1} with minimal polarization of 0.276 V at 0.1 A·g^{-1}, while maintaining good cycling stability after 1000 cycles. This work demonstrates the feasibility of regulating sulfur redox processes through modification of coordination environments of the single-atom catalysts within nitrogen, sulfur-doped porous carbon with well-developed porosity, which can simultaneously buffer volume expansion and enhance kinetics, affording a solution for building high-performance AZSBs.

2 Experimental section

2.1 Reagents

All analytical-grade reagents, including 2-methylimidazole (2-MIM, 99%), zinc nitrate hexahydrate ($Zn(NO_3)_2{\cdot}6H_2O$, 99%), zinc iodide (ZnI_2, 99%), $K_2S_2O_3$ (99%), ethanol (EtOH, 99.5%), methanol (MeOH, 99.5%), and polyvinylidene fluoride (PVDF), were purchased from Sinopharm Chemical Reagent Co., Ltd. and used as received without further purification.

2.2 Preparation of Zn SAs/NSC

A mixture of 1.0 g of as-synthesized ZIF-8 and 0.5 g of $K_2S_2O_3$ was initially ground in an agate mortar and then mechanically milled in a planetary ball mill at 360 rpm for 6 h. The homogenized precursor was transferred to an alumina crucible, and it was pyrolyzed in a tube furnace under an argon atmosphere. The temperature was raised to the target values (700, 800, or 900 °C) at a heating rate of 5 °C·min^{-1} and maintained for 2 h. The resulting black powder was first washed with 3 M HCl to remove metallic impurities. Subsequently, it was washed with carbon disulfide to eliminate elemental sulfur. Finally, the product was thoroughly rinsed by alternating deionized water and ethanol before drying. The final product was dried in a vacuum oven at 80 °C for 6 h to yield Zn SAs/NSC-*x* (*x* represents the carbonization temperature).

For comparison, a control sample (denoted as NPC) was prepared by directly carbonizing pristine ZIF-8 at 800 °C under identical conditions without $K_2S_2O_3$ addition.

2.3 Preparation of sulfur cathode

Sulfur was loaded into the Zn SAs/NSC host through a melt-diffusion method. 100 mg of Zn SAs/NSC-*x* was mixed with sulfur powder with a mass ratio of 1:1 and sealed in a stainless-steel autoclave, then heated at 160 °C in a muffle furnace for 6 h.

2.4 Electrochemical measurements

To prepare the working electrode, the as-obtained sample materials (Zn SAs/NSC-*x*/S) were mixed with conductive carbon black and a polytetrafluoroethylene (PTFE) binder at a mass ratio of 8:1:1. The mixture was ultrasonicated to form a homogeneous slurry, which was then coated onto a stainless-steel mesh. The sulfur loading was about 2 mg·cm^{-2}, and the electrode was dried at 80 °C. AZSBs were assembled in coin-cell configuration using the as-prepared cathode, a zinc foil (0.1 mm) as the anode, and a glass fiber separator, with 3 M $ZnSO_4$ + 0.05 M ZnI_2 aqueous solution as the electrolyte. It should be noted that to highlight the intrinsic activity of the Zn–N_4–S sites, a low ZnI_2 concentration (0.05 M) was deliberately used. Galvanostatic charge–discharge (GCD), cyclic voltammetry (CV), and electrochemical impedance spectroscopy (EIS) measurements were conducted using a CHI 660E electrochemical workstation. Cycle stability was evaluated using a Land test system, and galvanostatic intermittent titration technique (GITT) measurements were also performed. It should be noted that the specific capacity of the cathode was calculated based on the mass of loaded sulfur.

2.5 Pouch cell assembly

Similar to the coin-cell preparation, a homogeneous slurry containing different sample materials was coated onto pre-cut stainless-steel meshes (5 cm × 5 cm) with a sulfur loading of about 6 mg·cm^{-2}, followed by drying at 80 °C for 6 h. To prepare the gel electrolyte, 3 g of gelatin was dissolved in 12 mL of electrolyte (3 M $ZnSO_4$ + 0.05 M ZnI_2) under stirring at 60 °C for 2 h. The resulting gel was stored at 5 °C for 12 h. Finally, the pouch cell was assembled by stacking the gel electrolyte and zinc foil, and then sealed using an aluminum plastic film.

3 Results and discussion

As demonstrated in Fig. 1(a), this study develops a synthetic strategy using ZIF-8 as the precursor, where the introduction of $K_2S_2O_3$ simultaneously serves as a sulfur source for doping and creates a porous carbon framework. During pyrolysis, the imidazole rings of ZIF-8 cleave, generating N-active sites that coordinate with Zn^{2+} to form stable Zn–N_4 configurations. Concurrently, $K_2S_2O_3$ acts as a chemical activating agent, etching the carbon skeleton to create abundant hierarchical pores (micro-/mesopores). Sulfur species incorporate into the lattice, forming N–S bonds that break the symmetry of the conventional Zn–N_4 structure, ultimately yielding Zn SAs/NSC. This strategy overcomes the limitations of weakly polar Zn–N_4 configurations and the insufficient specific surface area/pore volume of conventional sulfur host materials.

The microstructural evolution of the ZIF-8-derived carbons was investigated by scanning electron microscopy (SEM), as shown in Fig. S1 in the Electronic Supplementary Material (ESM). The ZIF-8 precursor exhibited well-defined dodecahedral morphology with uniform particle size (100–200 nm) and smooth surfaces. Direct carbonization of ZIF-8 at 800 °C led to the complete collapse of the dodecahedral framework, forming irregular carbon aggregates (Fig. S2 in the ESM), which can be attributed to the explosive release of gases from ligand decomposition, causing framework rupture and particle agglomeration. When $K_2S_2O_3$ was introduced, the morphology of the resulting samples varied considerably with temperature. At 700 °C (Fig. S3 in the ESM), the material partially maintained polyhedral characteristics with smooth surfaces, while only some localized pores formed due to mild etching by $K_2S_2O_3$ at this temperature. As the temperature increased to 800 °C (Fig. 1(b) and Fig. S4 in the ESM), the surfaces underwent selective contraction and reconstruction, transforming from smooth to rough and porous. In addition, the edges experienced less contraction and remained recognizable while facets became concave, which is likely attributed to the anisotropic thermal stability of ZIF-8 crystals [41]. The resulting quasi-core–shell structure, featuring a porous shell and denser interior, facilitates full exposure of active sites and promotes ion diffusion. In contrast, after pyrolysis at 900 °C (Fig. S5 in the ESM), the original dodecahedral structure was completely destroyed, but instead, a large, smooth carbon aggregates were formed, which resulted from severe particle fusion at high temperatures. Transmission electron microscopy (TEM) image provides additional evidence for the quasi-core–shell architecture obtained at 800 °C (Fig. 1(c)). Such structural features not only offer sufficient space for sulfur loading but also help accommodate volume expansion during cycling [41]. High-resolution TEM (HRTEM) image (Fig. 1(d)) reveals an amorphous carbon matrix as evidenced by the absence of discernible lattice fringes, confirming that no metallic nanoparticles or crystalline phases were formed. Aberration-corrected high-angle annular dark-field scanning TEM (HAADF-STEM) image (Fig. 1(e)) directly presents isolated bright spots with sizes of 0.2–0.3 nm as highlighted by yellow circles, which is the typical characteristic of metal single atoms. No nanoparticle agglomeration was observed, confirming the uniform dispersion of Zn single atoms within the carbon matrix. Three-dimensional (3D) atomic distance distribution simulations (Fig. 1(f)) reveal a nearest-neighbor Zn–Zn separation of approximately 0.504 nm, with no significant signal at distances < 0.3 nm, providing direct evidence for the atomic dispersion of Zn species without metallic cluster formation. In addition, the element mapping images (Fig. 1(g)) indicate that the four elements C, N, S, and Zn are uniformly distributed within a scale of 200 nm. Inductively coupled plasma optical emission spectrometry (ICP-OES) analysis confirms the Zn contents in Zn SAs/NSC-*x* are in the range of 0.63 wt.%–3.63 wt.% (Fig. S6 in the ESM).

To investigate the atomic-scale coordination configuration and electronic properties of Zn species, X-ray absorption spectroscopy (XAS) measurement was performed. The X-ray absorption near-edge structure (XANES) spectrum of Zn SAs/NSC-800 (Fig. 1(h)) reveals an absorption edge position at 9661 eV, which is located between that of metallic Zn foil (9659 eV, zero valence) and ZnO (9663 eV, +2 valence), and slightly lower than that of zinc phthalocyanine (ZnPc) [42]. This indicates an oxidation state of the Zn atoms with Zn SAs/NSC-800 between 0 and +2. Besides, compared with the NPC, absorption edge of Zn SAs/NSC-800 shifts towards a lower binding energy, indicating a decrease in the valence state of Zn atoms. This might be due to the fact that sulfur

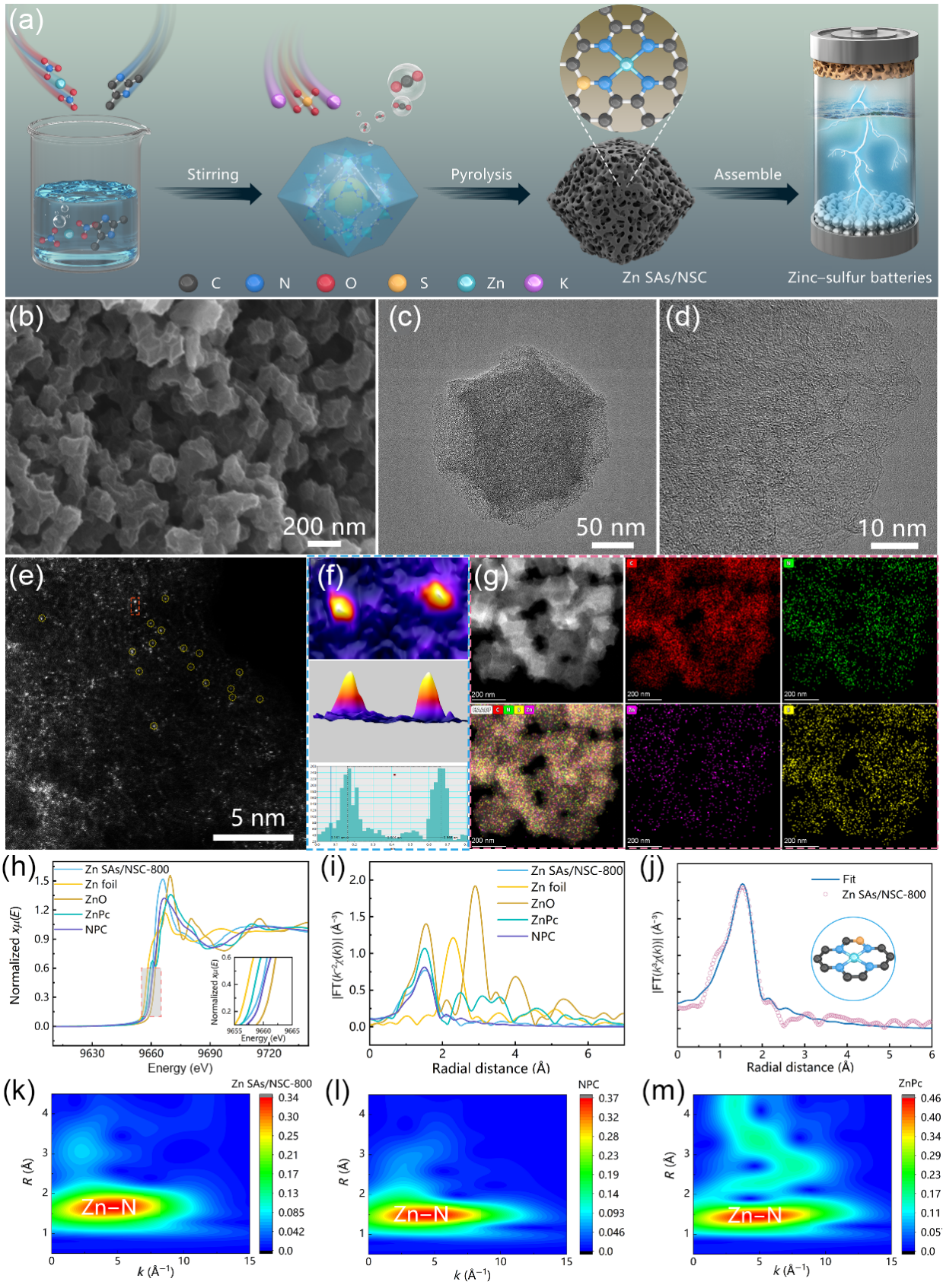

Figure 1 (a) Schematic illustration of the preparation process of Zn SAs/NSC. (b) SEM image, (c) TEM image, and (d) HRTEM image of the Zn SAs/NSC-800. (e) Aberration-corrected HAADF-STEM image of Zn atoms in the Zn SAs/NSC-800 and (f) the corresponding 3D fitting mapping. (g) The element mapping images and their overlays indicate that the four elements C, N, S, and Zn are uniformly distributed within a scale of 200 nm. (h) Zn K-edge XANES spectra. (i) FT of the extended EXAFS spectra. (j) FT and fitting curves of the EXAFS spectra. ((k)–(m)) Wave function distribution of Zn SAs/NSC, ZnO, and ZnPc.

can act as an electron donor, which increases the charge of adjacent Zn atoms [43]. In the Fourier transform (FT) extended X-ray absorption fine structure (EXAFS) spectra (Fig. 1(i)), Zn SAs/NSC-800 exhibits a single dominant peak at ~ 1.5 Å, attributed to the first coordination shell scattering of Zn. The peak position is intermediate between the Zn–N peak in ZnPc (1.45 Å) and the Zn–O peak in ZnO (1.55 Å). The absence of a Zn–Zn metallic bonding peak related to Zn foil (~ 2.3 Å) rules out the presence of Zn nanoparticles or metal clusters within Zn SAs/NSC-800 and NPC. In addition, the NPC exhibits a characteristic single peak for Zn–N bonds only at radial distances R = 1.9–2.0 Å, corresponding to Zn–N bonding in the first coordination sphere. In contrast, the radial distribution function (RDF) curve for Zn SAs/NSC-800 exhibits a weak signal at R = 2.5–3.0 Å that is absent in NPC sample, suggesting the presence of a second coordination layer interaction in the Zn coordination environment of Zn SAs/NSC-800. The peak shift to the right for Zn SAs/NSC-800 confirms again the slight increase in the Zn–N bond length (Fig. S7 in the ESM), which is in good agreement with the absorption edge position results. To identify the coordination configuration, the EXAFS spectra of Zn SAs/NSC-800 and NPC were fitted (Fig. 1(j) and Figs. S8 and S9 in the ESM). The EXAFS fitting results reveal NPC exhibiting a Zn coordination environment close to Zn–N_4 configuration with a coordination number of 4.0 ± 0.2, and the Zn atom's distance to the neighboring atom is 2.00 Å. For Zn SAs/NSC-800, although a similar coordination number of 4.0 ± 0.1 is obtained, the Zn atoms' distance to the neighboring atom slightly increased to 2.05 Å. Both of the Zn SAs/NSC-800 and NPC demonstrate dominant peaks at 1.5 Å, which are ascribed to the Zn–N coordination. The absence of Zn–S scattering paths at 1.7–1.8 Å confirms sulfur resides in the second coordination sphere, consistent with a Zn–N_4–S ternary structure model. Wavelet transform (WT) analysis, which provides a two-dimensional representation in k- and R-spaces, was employed to distinguish the contributions from different scattering atoms (Figs. 1(k)–1(m) and Fig. S10 and Table S1 in the ESM). The WT contour plot of Zn SAs/NSC-800 and NPC show a single intensity maximum at photoelectron wave vector magnitude (k) ≈ 5.8 $Å^{-1}$ and R ≈ 1.5 Å (Fig. 1(l)), which is consistent with that of ZnPc (Fig. 1(m), k ≈ 5.6 $Å^{-1}$) but distinctly different from the Zn–O scattering in ZnO (Fig. S10 in the ESM, k ≈ 7.2 $Å^{-1}$) and the Zn–Zn scattering in Zn foil (Fig. S10 in the ESM, k ≈ 8.5 $Å^{-1}$). These results directly confirm that the first Zn coordination shell in Zn SAs/NSC-800 and NPC, which consists of N atoms without long-range ordered metallic or oxide bonds, further validates the single-atom Zn–N_4 coordination configuration. Additionally, the WT contour plot (Fig. 1(l)) reveals a weak secondary peak at k = 4.5 $Å^{-1}$ and R = 2.6 Å, which is consistent with the theoretical wave vector (k = 4–5 $Å^{-1}$) for N–S scattering, while this signal is absent in NPC, suggesting the presence of sulfur in the second coordination shell [42, 43]. Additionally, the weak signal at R = 3.0–3.5 Å for the Zn SAs/NSC-800 corresponds to the theoretical value of the indirect distance between the Zn atom and the sulfur atom, further supporting the sulfur atom position in the second coordination sphere.

N_2 adsorption and desorption analysis were first performed to evaluate the textural properties of the resulting samples. As shown in Fig. 2(a), all samples before sulfur loading exhibit combined Types I and IV isotherms [44], indicating the presence of abundant micropores and mesopores. Prior to sulfur loading, the specific surface areas of Zn SAs/NSC-700, Zn SAs/NSC-800, and Zn SAs/NSC-900 were 1531.5, 2135.5, and 2521.2 $m^2 \cdot g^{-1}$, respectively. These values decreased significantly to 41.2, 44.1, and 41.1 $m^2 \cdot g^{-1}$ after sulfur impregnation, confirming the successful infusion of molten sulfur into the nanopores. The corresponding pore size distribution curves shown in Fig. 2(b) demonstrate that, before sulfur loading, all three Zn SAs/NSC samples exhibit abundant hierarchical pores. Specifically, Zn SAs/NSC-800 displays three main pore sizes at 0.812, 1.235, and 2.965 nm; Zn SAs/NSC-700 shows two main pore peaks at 0.545 and 2.195 nm; while Zn SAs/NSC-900 presents three prominent pore size distributions at 0.853, 1.021, and 2.901 nm. The large and specific surface areas, wide pore size distribution of Zn SAs/NSC-800 can alleviate strain induced by volume changes during cycling as well as provide more active sites, thereby enhancing the electrochemical performance of the resulting AZSBs. Furthermore, the microporous structure was largely eliminated after sulfur loading, while only some mesopores and macropores remained, further confirming the successful confinement of sulfur within the carbon hosts. As shown in Fig. 2(c), the X-ray diffraction (XRD) patterns of all samples exhibit a broad and low-intensity diffraction peak near 23°, implying their amorphous nature. Notably, no distinct crystalline diffraction peaks corresponding to zinc species are observed, indicating that zinc is atomically dispersed without forming nanoparticles, which is consistent with the SEM and TEM results. The Raman spectra (Fig. 2(d)) display two characteristic vibration modes commonly found in carbon materials. Peak deconvolution reveals four sub-peaks located at ~ 1205 cm^{-1} (I peak), ~ 1343 cm^{-1} (D peak), ~ 1487 cm^{-1} (D" peak), and ~ 1583 cm^{-1} (G peak). The intensity ratio of the D band to the G band (I_D/I_G) serves as an indicator for the defect density within carbon materials [45]. The calculated I_D/I_G ratios for Zn SAs/NSC-700, Zn SAs/NSC-800, and Zn SAs/NSC-900 are 1.74, 1.88, and 2.29, respectively (Table S2 in the ESM). The increased defect density helps expose more edge carbon sites, which can facilitate ion migration and reaction kinetics, thereby potentially enhancing the specific capacity and rate capability of the AZSBs. X-ray photoelectron spectroscopy (XPS) measurement confirms that the surfaces of the Zn SAs/NSC-700, Zn SAs/NSC-800, and Zn SAs/NSC-900 samples are primarily composed of five elements: C, N, O, S, and Zn (Fig. S11 in the ESM). As shown in Fig. S12 in the ESM, the high-resolution C 1s spectra can be deconvoluted into three characteristic peaks at 284.8 eV (C–C), 286.4 eV (C–N/C–O/C–S), and 291.2 eV (O–C=O), confirming the successful doping of N and S heteroatoms into the carbon matrix. The N 1s spectra (Fig. 2(e)) can be further fitted into five components assigned to pyridinic N (N-6, 398.3 eV), N–S bonds (399.2 eV), pyrrolic N (N-5, 400.2 eV), graphitic N (N-Q (Q refers to quaternary), 401.6 eV), and oxidized N (N–O, 404.3 eV) [46]. The identification of N–S bonds verifies the successful bonding between S atoms and N sites, which breaks the symmetry of the Zn–N_4 structure and modulates the electronic structure of the Zn single atom centers, contributing to enhanced electrocatalytic activity. It is noteworthy that the relative content of N–S bonds increases with the pyrolysis temperature, likely due to the volatilization of some Zn atoms at higher temperatures, creating more nitrogen vacancies, thereby providing more opportunities for S atoms to bond with N sites. Besides, the sulfur content in Zn SAs/NSC-800 is 3.93 at.%, which is significantly higher than that in Zn SAs/NSC-700 (0.58 at.%) and Zn SAs/NSC-900 (1.80 at.%) (Table S3 in the ESM). The O 1s spectra (Fig. 2(f)) are fitted with

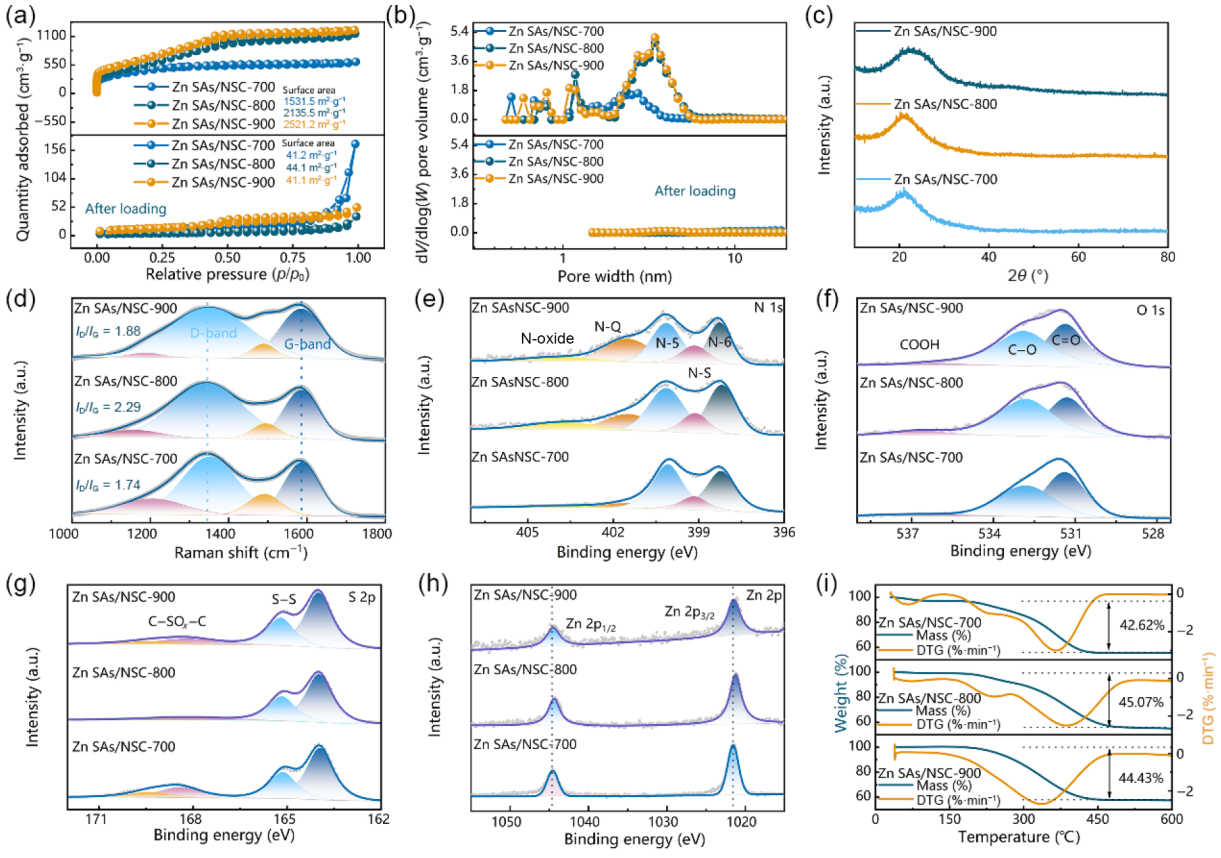

Figure 2 (a) N_2 isotherms and (b) the corresponding pore size distribution curves before and after sulfur loading. (c) XRD patterns. (d) Raman spectra. ((e)–(h)) High-resolution N 1s, O 1s, S 2p, and Zn 2p spectra. (i) TGA curves of the samples after sulfur loading.

three peaks at 531.4 eV (C=O), 532.9 eV (C–O), and 536.4 eV (–COOH), indicating the presence of abundant oxygen-containing functional groups on the material surface, which can improve electrode wettability and electrochemical performance. The S 2p spectra (Fig. 2(g)) show three main peaks at binding energies of 164.1 eV (S $2p_{3/2}$), 165.2 eV (S $2p_{1/2}$), and 168.4 eV (C–S–O_x–C), further confirming the successful doping of S and its bonding state within the carbon framework [47]. Furthermore, the Zn 2p high-resolution spectra (Fig. 2(h)) exhibit characteristic peaks at 1021.7 eV (Zn $2p_{3/2}$) and 1045.1 eV (Zn $2p_{1/2}$), with no signals from other zinc species detected, indicating that Zn is stably present in the carbon carrier as single atoms. Especially, with the N–S content increased, the Zn 2p spectra shift towards a lower binding energy due to electron injection from the second-shell sulfur atoms, which is consistent with the XAS results. Thermogravimetric analysis (TGA) was performed to quantify the sulfur content in Zn SAs/NSC-*x*/S. As shown in Fig. 2(i), the mass of all samples remains stable below 100 °C. When the temperature exceeds 200 °C, the mass decreases sharply due to the volatilization of elemental sulfur. The mass curve stabilizes again by 600 °C, indicating complete sulfur removal. The calculated sulfur contents for Zn SAs/NSC-700, Zn SAs/NSC-800, and Zn SAs/NSC-900 are 42.6%, 45.1%, and 44.4%, respectively, demonstrating similar sulfur loadings across materials synthesized at different pyrolysis temperatures.

Building upon the aforementioned physicochemical properties of the Zn SAs/NSC material, including its high specific surface area, abundant porous structure, Zn–N_4–S active sites, and N, S doping, it is expected to be promising sulfur host for AZSBs. Figure 3(a) presents the CV curves of NPC and Zn SA/NSC host materials. All samples exhibit a distinct oxidation peak at ~ 1.2 V, corresponding to the solid–solid conversion of ZnS to S_8. Notably, the Zn SAs/NSC samples (700, 800, and 900 °C) display significantly sharper and more positive reduction peaks compared to the pristine NPC, suggesting the enhanced reversibility. This confirms that Zn–N_4–S ternary structure within N, S-doped carbon host can accelerate the redox kinetics of sulfur by lowering the energy barrier for solid–solid phase transition. Specifically, in comparison with NPC, the reduction peak potential of Zn SAs/NSC-800 shifted positively by 0.34 V, while the oxidation peak potential shifted negatively by 0.03 V, resulting in the smallest peak potential separation (ΔE) of only 0.53 V. This confirms the synergistic effect of Zn single atoms and N–S co-doping in significantly reducing the reaction energy barrier. Scan rate-dependent contour plots of CV patterns further demonstrated the strongest current response within the voltage ranges of 1.0–1.4 and 0.6–0.8 V, highlighting the superior solid–solid conversion kinetics of the Zn SAs/NSC-800 host (Fig. 3(b)). Analysis of the GCD profiles systematically evaluates the electrochemical performance of the four cathode materials (Zn SAs/NSC-700, Zn SAs/NSC-800, Zn SAs/NSC-900, and NPC). In terms of specific capacity, Zn SAs/NSC-800 delivers the highest reversible capacity, approaching 1610 mAh·g^{-1}, which is very close to its theoretical value (1675 mAh·g^{-1}) and significantly superior to those of Zn SAs/NSC-700 (988.3 mAh·g^{-1}), Zn SAs/NSC-900 (1241 mAh·g^{-1}), and NPC (1369 mAh·g^{-1}) (Fig. 3(c) and Figs. S13–S16 in the ESM). This indicates that the unique structure formed at the 800 °C pyrolysis temperature is most favorable for efficient sulfur utilization and capacity release. Regarding the

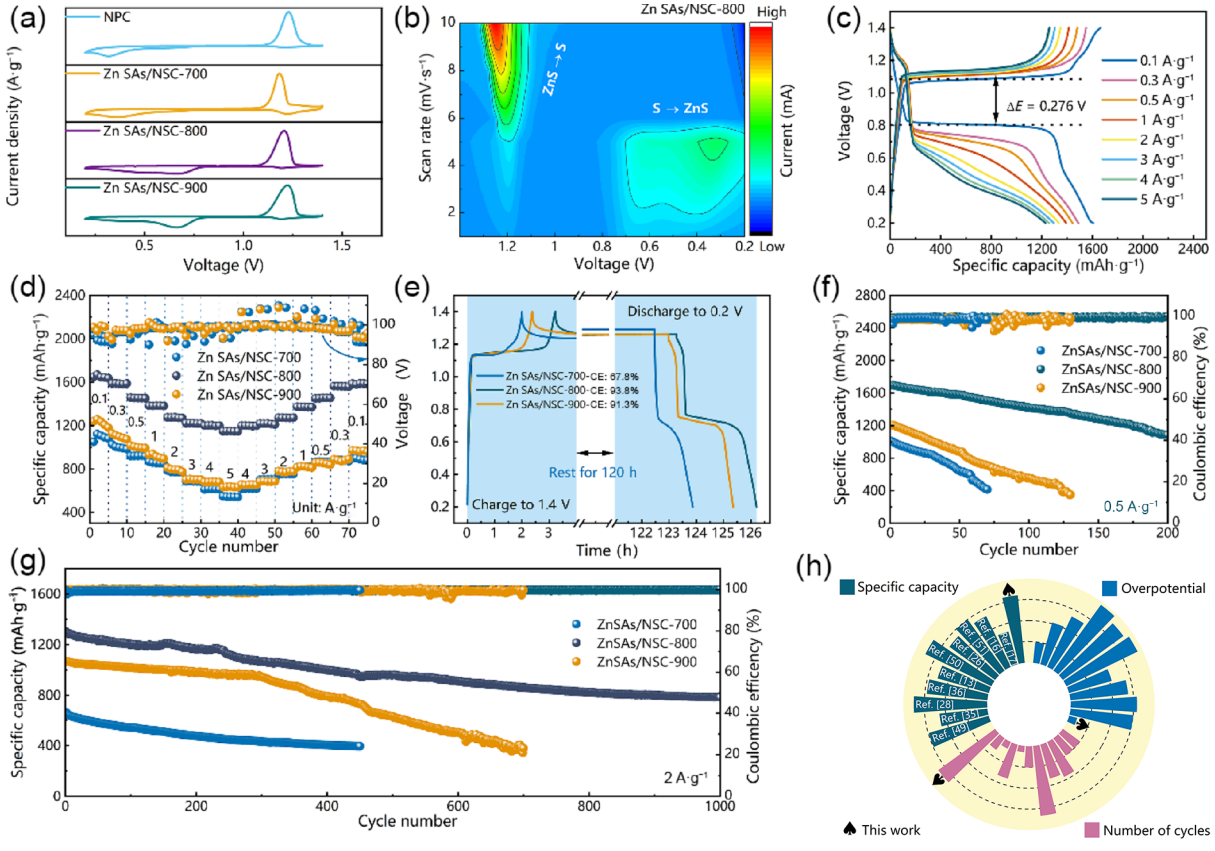

Figure 3 (a) CV curves of different cathode materials. (b) Contour plots of CV patterns for Zn SAs/NSC-800-based host with various scan rates. (c) GCD curves for Zn SAs/NSC-800-based host at different current densities. (d) Rate capability. (e) Self-discharge test curves of different cathode materials. ((f) and (g)) Cycling stability of Zn SAs/NSC-800-based host at 0.5 and 2 A·g^{-1}. (h) Comparison the electrochemical performance of Zn SAs/NSC-800-based host with other cathodes.

charge–discharge plateaus, all materials exhibit two distinct voltage plateaus corresponding to the typical solid–solid conversion reaction [45]. Notably, Zn SAs/NSC-800 not only possesses the longest and flattest discharge plateaus, suggesting a stable and highly efficient conversion process, but also demonstrates the smallest voltage gap (ΔV = 0.276 V) between charge and discharge profiles. This minimal polarization unequivocally reveals the most rapid electrode reaction kinetics, the lowest internal resistance, and superior reversibility for Zn SAs/NSC-800. Moreover, even at a high current density of 5 A·g^{-1}, it maintained a capacity of 1229.1 mAh·g^{-1}, corresponding to a capacity retention of 76.3%, demonstrating excellent rate capability (Fig. 3(d)). Zn SAs/NSC-800 achieves good rate performance due to a capacitive-dominated storage mechanism, which is enabled by its high-surface-area, abundant porous structure that facilitates rapid surface redox reactions. As the current density increased from 0.1 to 5 A·g^{-1} and then returned to 0.1 A·g^{-1}, Zn SAs/NSC-800 recovered a capacity of 1586.6 mAh·g^{-1}, significantly higher than those of Zn SAs/NSC-700 (897.9 mAh·g^{-1}) and Zn SAs/NSC-900 (971.7 mAh·g^{-1}), demonstrating its superior structural stability and reversibility. In contrast, NPC exhibits the largest polarization up to 0.512 V and an inferior discharge plateau, indicating its sluggish kinetics. Self-discharge tests showed that after charging to 1.4 V and resting for 120 h, the Zn SAs/NSC-800-based cathode still delivered a discharge capacity of 1485.6 mAh·g^{-1}, with a Coulombic efficiency surpassing that of the other samples (Fig. 3(e)). In terms of cycling stability (Figs. 3(f) and 3(g)), Zn SAs/NSC-800-based cathode retained 64% of its initial capacity after 200 cycles at 0.5 A·g^{-1}, while maintaining a Coulombic efficiency above 99%. Even after 1000 cycles at 2 A·g^{-1}, with an average capacity decay rate of only 0.523 mAh·g^{-1} per cycle, a capacity retention of 60% was achieved. Post-cycling SEM measurement confirms that the Zn SAs/NSC-800 cathode maintains its integral porous architecture after 1000 cycles, providing direct morphological evidence for the structural robustness that underpins its exceptional long-term cycling stability (Fig. S17 in the ESM). While the inherently poor reversibility of the S/S^{2-} redox reaction and high oxidation barrier of ZnS represent a fundamental challenge for capacity retention in AZSBs, the asymmetric Zn–N_4–S sites coupled with a high-surface-area porous carbon matrix in Zn SAs/NSC-800 significantly mitigate this issue by enhancing reaction kinetics and reversibility, resulting in superior cycling stability relative to the Zn SAs/NSC-700 and Zn SAs/NSC-900-based cathode as well as exceed those of most reported sulfur-based cathode materials, such as sulfur and nitrogen co-doped carbon nanofibers [48], FeN_4 single sites/nitrogen-doped carbon cloth [35], Ketjen black [28], biomass-derived porous carbon matrix incorporating single-atom cobalt [36], hollow nanocubes of $Ni_xFe_yO_4$ mixed metal oxide [13], Te-incorporated S cathode [26], Se-incorporated S cathode [49], carbonized bacterial cellulose and partially alloyed with Co [16], and zinc sulfide [17] (Fig. 3(h) and Table S4 in the ESM). 3D hierarchical porous structure of Zn SAs/NSC-800 enables efficient sulfur storage and volume buffering and Zn–N_4–S sites with N, S co-doping enhance the reaction kinetics with an overall effect on the electrochemical performance [31, 50–52].

To further demonstrate its practical application, the AZSBs

pouch cell (sulfur loading of 6.1 mg·cm^{-2}) with Zn SAs/NSC-800/S as the cathode was assembled. As shown in Fig. 4(a), the resulting AZSBs pouch cell can offer an initial open-circuit voltage of 1.155 V. To evaluate its mechanical flexibility, cycling performance (at 0.5 A·g^{-1}) under original conditions and after bending at 45°, 90°, 135°, 180°, and subsequent recovery indicating that the specific capacity can remain 1200–1500 mAh·g^{-1} with Coulombic efficiency above 95% at all states (Fig. 4(b) and Fig. S18 in the ESM). The GCD curves in Fig. 4(c) reveal that typical discharge and charge plateaus are about 0.8 and 1.2 V, respectively, as the current densities increased from 0.1 to 5 A·g^{-1}. A high specific capacity of 1418.2 mAh·g^{-1} is achieved at 0.1 A·g^{-1}, which is close to the theoretical capacity of sulfur. This corresponds to a cell specific energy of around 35.5 Wh·kg^{-1} (total pouch cell mass). As the current density increased to 5 A·g^{-1}, a high level of 935.4 mAh·g^{-1} is retained, confirming excellent rate capability. Moreover, the pouch cell also exhibits a capacity retention of over 46% after 200 cycles (initial capacity ~ 1300 mAh·g^{-1}) with Coulombic efficiency above 98% at 1 A·g^{-1} (Fig. 4(d)), indicating its long-term cycling stability and high sulfur utilization. For practical application, a single pouch cell successfully powers a red LED panel (Figs. 4(e)–4(g)), and still maintains stable operation even after deliberate cutting (Figs. 4(f) and 4(g)), verifying its safety and practical power supply.

To better understand the mechanism behind the enhanced electrochemical performance of the Zn SAs/NSC-800-based cathode, the kinetics analysis was conducted. CV measurements (Fig. 5(a)) revealed four distinct redox peaks (Peaks 1–4) within the scan rate range of 0.2–1.0 mV·s^{-1}. The relationship between peak current (i) and scan rate (v) was examined via the following equation [53]

$$i = av^b \quad (1)$$

where a and b stand for the adjustable parameters.

The calculated b-values for Peaks 1–4 were 0.71, 0.99, 0.63, and 0.98, respectively (Fig. 5(b)). The b-values close to 1 for the reduction Peak 2 (~ 0.8 V) and the oxidation Peak 3 (~ 1.4 V) indicate a predominantly surface-capacitive controlled process. In contrast, the b-values for Peaks 1 and 4 (0.63–0.71) suggest a mixed control involving diffusion. The capacitive and diffusion-controlled contributions were deconvoluted using Eq. (2) [53]

$$i = k_1 v + k_2 v^{1/2} \quad (2)$$

where k_1 and k_2 represent the surface-controlled (capacitive) and diffusion-controlled contribution coefficients, respectively.

The results demonstrate that Zn SAs/NSC-800-based cathode exhibits a capacitive contribution increasing from 86% at 0.2 mV·s^{-1} to 97% at 1.0 mV·s^{-1} (Figs. 5(c) and 5(d)), which is larger than that of Zn SAs/NSC-700 and Zn SAs/NSC-900-based cathode (Figs. S19 and S20 in the ESM).

EIS plots (Fig. 5(e)) indicate a substantially lower charge transfer resistance (R_{ct} = 6.6 Ω) for Zn SAs/NSC-800 compared to the Zn SAs/NSC-700 (14.2 Ω) and Zn SAs/NSC-900 (17.3 Ω) samples. Warburg impedance analysis (imaginary impedance (Z'') vs. inverse square root of angular frequency ($\omega^{-1/2}$), Fig. S21 in the ESM) demonstrates that Zn SAs/NSC-800-based cathode yielded a lower slope of the linear fitting curve in the low-frequency range than that of the other cathodes. The distribution of relaxation times (DRT) curves of Zn SAs/NSC-700, Zn SAs/NSC-800, and Zn SAs/NSC-900 reveal that the electrochemical kinetics of the

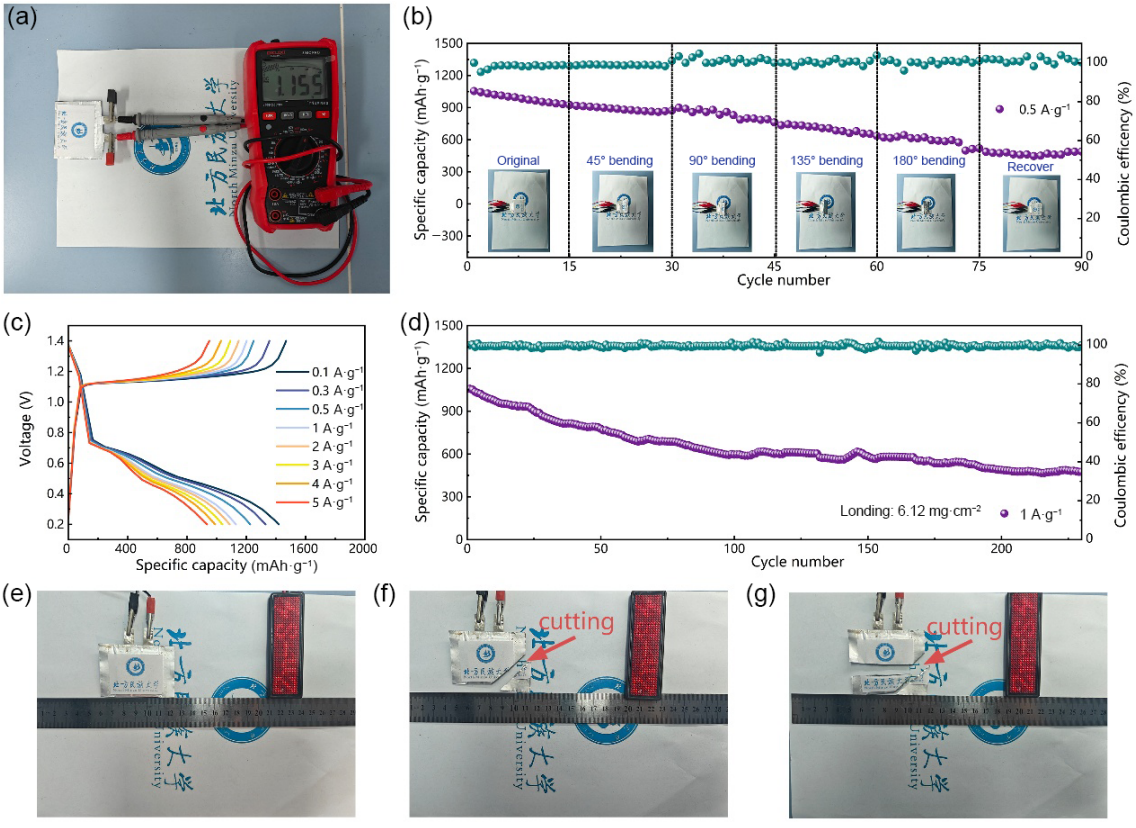

Figure 4 (a) Photographs of the pouch battery for Zn SAs/NSC-800-based host and its open-circuit voltage (OCV) monitoring. (b) Cycling performance at different bending angles. (c) GCD curves at different current densities and (d) Cycling stability at 1 A·g^{-1}. ((e)–(g)) Demonstrations of the pouch battery powering light-emitting diodes (LEDs) and maintaining stable operation even under physical damage.

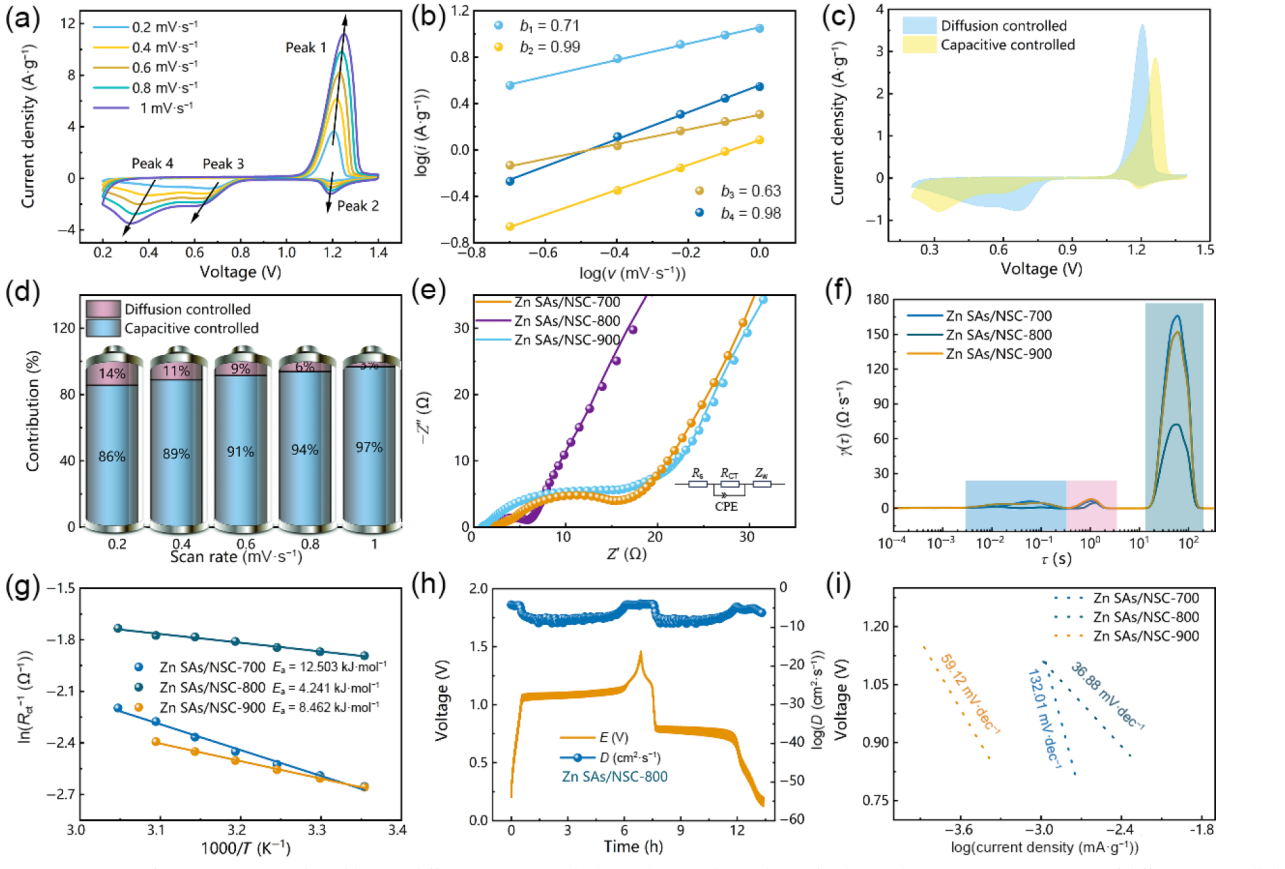

Figure 5 (a) CV curves of Zn SAs/NSC-800-based host at different scan rates. (b) log(*i*)–log(*v*) relationships of redox peak currents. (c) Separation of diffusion-controlled and capacitive-controlled capacity contributions. (d) Bar chart of the proportion of capacitive-controlled contribution at different scan rates. (e) EIS Nyquist plots. (f) Distribution of relaxation times (DRT) curves. (g) Arrhenius plots for activation energy calculation. (h) GITT curves and the corresponding ion diffusion coefficients. (i) Comparison of Tafel slopes.

cathodes are significantly regulated by the synthesis temperature, characterized by three relaxation processes (Fig. 5(f)): a weak peak in the high-frequency region (high-frequency relaxation time (τ_1) = 10^{-2}–10^{-1} s) corresponding to charge transfer, a moderately intense peak in the medium-frequency region (medium-frequency relaxation time (τ_2) = 1 s) assigned to surface adsorption/desorption, and a dominant strong peak in the low-frequency region (low-frequency relaxation time (τ_3) = 10–100 s) attributed to diffusion-controlled processes [19, 20, 54]. Among them, Zn SAs/NSC-800 exhibits a significantly lower relaxation-time distribution intensity ($\gamma(\tau)$ = 25) compared to Zn SAs/NSC-700 ($\gamma(\tau)$ = 40, relaxation time (τ) = 50 s) with a left-shifted peak position in the low-frequency diffusion peak (τ_3 = 20 s), indicating its reduced diffusion resistance and accelerated kinetics. Besides, it also displays the lowest intensity ($\gamma(\tau)$ = 5) in the high-frequency charge transfer peak (τ_1), which is significantly lower than those of Zn SAs/NSC-700 ($\gamma(\tau)$ = 12) and Zn SAs/NSC-900 ($\gamma(\tau)$ = 18), corresponding to the minimum R_{ct}. Moreover, Zn SAs/NSC-800-based cathode also presents the lowest intensity with a symmetric shape of the medium-frequency adsorption peak (τ_2 = 1 s), indicating stable surface reactions. Additionally, the activation energy (E_a) derived from the Arrhenius plot (Fig. 5(g) and Fig. S22 in the ESM) was 4.24 kJ·mol^{-1}, which is lower than that of the Zn SAs/NSC-700 (12.5 kJ·mol^{-1}) and Zn SAs/NSC-900 (8.46 kJ·mol^{-1}). GITT tests (Fig. 5(h) and Fig. S23 in the ESM) further demonstrated that Zn SAs/NSC-800 exhibits the smallest voltage polarization (ΔE = 0.18 V) and the most stable diffusion coefficient between 1.28×10^{-4} and 1.09×10^{-9} cm^2·s^{-1} as compared with the Zn SAs/NSC-700 (3.61×10^{-11} to 2.15×10^{-14} cm^2·s^{-1}) and Zn SAs/NSC-900 (3.75×10^{-7} to 7.55×10^{-12} cm^2·s^{-1}). The Tafel slope for Zn SAs/NSC-800 (36.88 mV·dec^{-1}, Fig. 5(i) and Fig. S24 in the ESM) was lower than that of the Zn SAs/NSC-700 (59.12 mV·dec^{-1}) and Zn SAs/NSC-900 (132.01 mV·dec^{-1}) samples, indicating optimized sulfur reduction reaction (SRR) kinetics. These results demonstrate that the synergistic effects of the hierarchical pore structure (micropores–mesopores–macropores), Zn–N_4–S sites, and N, S heteroatom doping of Zn SAs/NSC-800-based cathode can boost the diffusion and charge transfer kinetics by reducing charge transfer and ion diffusion barriers.

To gain comprehensive insights into the structural evolution and energy storage mechanisms of the Zn SAs/NSC-800 host material in AZSBs, we conducted *ex-situ* XRD and XPS measurements to track phase transformations and valence state changes at various electrochemical states (Fig. 6(a)). *Ex-situ* XRD patterns (Fig. 6(b)) reveal no crystalline diffraction peaks corresponding to S_8 across all states, confirming that sulfur exists in a highly dispersed amorphous form. Upon discharge to the endpoint (State C), a characteristic (111) peak of ZnS (PDF#05-0566) emerged at 2θ = 28.5°, which completely disappeared when charged to the endpoint (State F) [34]. No crystalline diffraction signals from polysulfides were detected, indicating a solid–solid transformation pathway involving "amorphous sulfur → ZnS → amorphous sulfur." Further evidence was provided by *ex-situ* S 2p XPS spectra (Fig. 6(c)). The S 2p spectra at State A were dominated by the S–S bond of amorphous

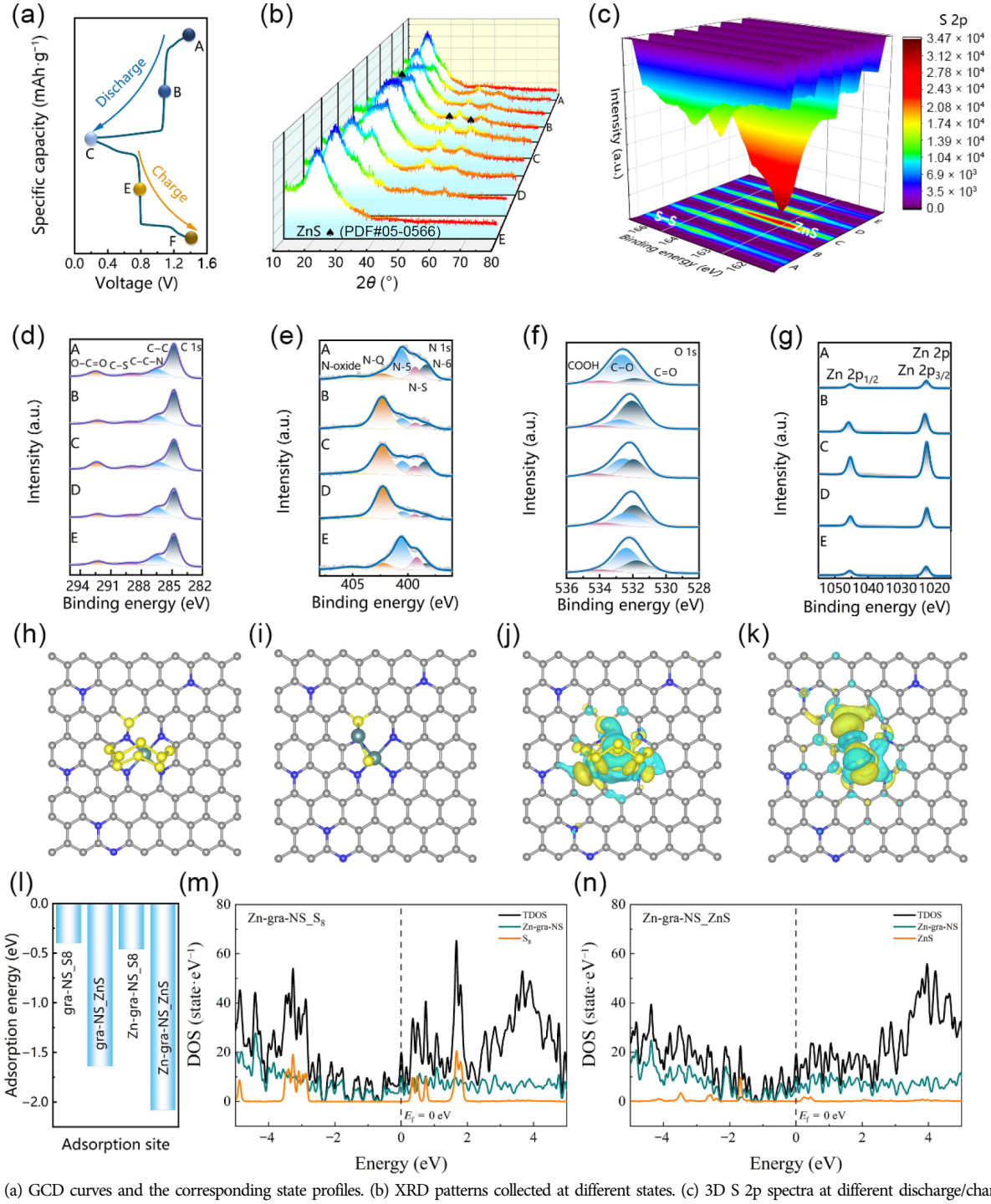

Figure 6 (a) GCD curves and the corresponding state profiles. (b) XRD patterns collected at different states. (c) 3D S 2p spectra at different discharge/charge states. ((d)–(g)) High-resolution XPS spectra of (d) C 1s, (e) N 1s, (f) O 1s, and (g) Zn 2p at various states. ((h)–(k)) The adsorption configurations and the corresponding differential charge density diagrams of ((h) and (i)) S_8 and ((j) and (k)) ZnS on the Zn-gra-NS surface. (l) Adsorption energy comparison of different intermediates on various substrates. ((m) and (n)) DOS of (m) S adsorption and (n) ZnS adsorption on Zn-gra-NS substrates.

sulfur (164.0 eV). At State C, the signal completely transitioned to the S^{2-} peak of ZnS (161.8 eV) [24] and reverted to amorphous sulfur at State F. Besides, no S 2p signals in the 162.5–163.5 eV can be detected, revealing the absence of soluble polysulfides (S_x^{2-}) [25, 55]. Furthermore, the persistent intensity of the C–S–C bond at 285.8 eV in C 1s spectra throughout cycling confirmed the effective physical confinement of sulfur species within the carbon matrix (Fig. 6(d)). Concurrently, N 1s spectra revealed a reversible modulation of nitrogen functionalities with approximately 15% attenuation in pyridinic N (398.4 eV) and N–S bond (399.2 eV) intensities during discharge, followed by partial recovery upon charging (Fig. 6(e)), demonstrating the participation of nitrogen sites in the solid–solid transformation process [28, 56]. In contrast, the obvious change of O 1s spectra only occurs during the first discharge process, indicating that it does not directly participate in the electrochemical reaction [57] (Fig. 6(f)). Importantly, Zn 2p

spectra remained almost unchanged at all states, indicating the structural integrity of Zn–N_4 centers during the solid-state conversion reactions (Fig. 6(g)). The observed upward shift in Zn 2p binding energy at point B reflects a transient decrease in electron density at the Zn–N_4–S site, as it donates electrons to activate the adsorbed S_8 molecule. These findings collectively demonstrate that the energy storage mechanism of the AZSBs with the Zn SAs/NSC-800 cathode involves a direct solid–solid reaction between amorphous sulfur and Zn^{2+}, assisted by Zn–N_4–S sites within N, S-doped carbon to form ZnS during discharging, while the ZnS decomposes back to amorphous sulfur during charging.

To elucidate the effects of Zn–N_4–S sites within N, S-doped carbon on the kinetically enhanced electrochemical performance, density functional theory (DFT) calculations were performed to compare the adsorption energies (E_{ads}) of S_8 and ZnS on nitrogen–sulfur co-doped graphene (gra-NS) and N, S-doped carbon with Zn–N_4–S sites (Zn-gra-NS) (Figs. 6(h) and 6(i) and Fig. S25 in the ESM). The calculation results revealed that the E_{ads} of gra-NS for S_8 was –0.40 eV, and for ZnS it was –1.64 eV. The E_{ads} of Zn-gra-NS for S_8 increased slightly to –0.46 eV after introducing Zn–N_4–S sites, but the E_{ads} for ZnS was significantly increased to –2.08 eV. These results indicate that the incorporation of Zn–N_4–S sites selectively strengthens the chemical adsorption capability towards ZnS, while its effect on S_8 adsorption remains relatively weak. Charge density difference analysis visually reveals the electron transfer behavior between sulfur species and the substrate surface (Figs. 6(j) and 6(k)). For the gra-NS system (Fig. S25 in the ESM), only weak charge accumulation (yellow regions) and depletion (blue regions) were observed near the pyridinic N atoms upon S_8 adsorption, indicating that the weak interaction with negligible electron transfer resulting from van der Waals forces [19]. For ZnS adsorption, localized charge rearrangement occurred between the N atoms and the S atoms of ZnS, but the magnitude of charge density variation was minimal, which is consistent with the moderate adsorption energy (–1.64 eV). On the contrary, the electron transfer behavior was significantly enhanced after introducing Zn–N_4–S sites (Zn-gra-NS). A distinct charge accumulation bridge formed between the Zn atom and the S_8 molecule, with electrons transferring from Zn to S, while Zn–S–Zn charge channel formed between the Zn–N_4 site and ZnS. The charge accumulation region expanded across the entire adsorption interface compared to the gra-NS system, consistent with the significantly enhanced adsorption energy (–2.08 eV) (Fig. 6(l)). Moreover, the density of states (DOS) analysis was conducted to reveal distinct electronic interactions with S_8 molecule and ZnS. For S_8 molecules, the DOS profiles of gra-NS show overlapping between the gra-NS valence band and sulfur states near the Fermi level (E_f = 0 eV), indicating electronic hybridization at the interface (Fig. S26 in the ESM). In contrast, the Zn-gra-NS exhibits enhanced overlapping between Zn-gra-NS and S_8 molecules, indicating that the introduced Zn–N_4–S sites enhance electronic coupling (Fig. 6(m)). For ZnS, the gra-NS/ZnS displays discrete DOS features with limited overlap between gra-NS and ZnS near the Fermi level. Conversely, the Zn-gra-NS/ZnS system shows a broader and more pronounced DOS overlap between the Zn-gra-NS and ZnS, with significant state density contributions from Zn-gra-NS near the Fermi level (Fig. 6(n)). This enhanced orbital hybridization directly leads to the increased ZnS adsorption energy (–2.08 eV), which is consistent with charge density difference analysis. These results indicate that the introduction of Zn–N_4–S sites modulates the electronic structure of the Zn SAs/NSC-800, leading to strengthened interfacial electronic interactions with both S_8 and ZnS compared to the pristine gra-NS. Therefore, the favorable kinetics of the solid–solid transformation can be attributed to these specific electronic structure characteristics of Zn SAs/NSC-800-based cathode.

4 Conclusions

In summary, we have successfully developed asymmetric Zn–N_4–S sites within N, S-doped porous carbon matrix as a superior sulfur cathode for AZSBs. Using a facile $K_2S_2O_3$-assisted pyrolysis method, Zn SAs/NSC-800 with large specific surface that can accelerate reaction kinetics and buffer volume changes simultaneously, which in turn addresses the major limitations of sulfur-based cathodes. Notably, the conventional Zn–N_4 configuration through second-sphere sulfur doping breaks the electronic symmetry. The resulting Zn–N_4–S sites function as highly polar and efficient active centers to reduce the energy barrier and enhance reaction kinetics of the solid–solid conversion, which is confirmed by DFT calculations. Consequently, the Zn SAs/NSC-800-based cathode delivers exceptional electrochemical performance, including a near-theoretical capacity of 1610.6 mAh·g^{-1}, an ultralow polarization of 0.276 V, and remarkable cycling stability with 60% capacity retention over 1000 cycles. *Ex-situ* spectroscopic analyses further demonstrate a direct solid–solid conversion pathway between amorphous S and ZnS. The good electrochemical performance of Zn SAs/NSC-800-based cathode stems from the effective synergy between the hierarchical porous architecture and the Zn–N_4–S sites. This work not only presents a high-performance host for sulfur loading but also affords a facile way to tailor the coordination microenvironment of metal single atoms for AZSBs.

Electronic Supplementary Material: Supplementary material (including DFT calculation; detailed synthesis process; additional SEM, XAS, XPS, and Raman results; CV, GCD, EIS, GITT curves; theoretical simulation diagrams; and a performance comparison table with reported cathode materials) is available in the online version of this article at https://doi.org/10.26599/NR.2026.94908560.

Data availability

All data needed to support the conclusions in the paper are presented in the manuscript and the Electronic Supplementary Material. Additional data related to this paper may be requested from the corresponding author upon request.

Acknowledgements

The authors are grateful for the financial support from the National Natural Science Foundation of China (No. 22365001) and the Natural Science Foundation of Ningxia (No. 2024AAC03150).

Declaration of competing interest

All the contributing authors report no conflict of interests in this work.

Author contribution statement

Z. S. W.: Data curation, experimental design, investigation, writing original draft. X. Y. Y.: Data curation, validation, formal analysis. G. C. Z.: Investigation, visualization, partial data analysis. D. W. W.: Conceptualization, project administration, supervision, funding

acquisition, reviewing and editing manuscript. Y. H. C.: Software, data curation. All the authors have approved the final manuscript.

Use of AI statement

None.

References

[1] Nanda, J.; Kalnaus, S. Cracking the failure of lithium batteries. *Science* **2025**, *388*, 255.

[2] Mahmood, A.; Bai, Z.; Wang, T.; Lei, Y. J.; Wang, S. J.; Sun, B.; Khan, H.; Khan, K.; Sun, K. N.; Wang, G. X. Enabling high-performance multivalent metal-ion batteries: Current advances and future prospects. *Chem. Soc. Rev.* **2025**, *54*, 2369–2435.

[3] Nykvist, B. On par with lithium-ion. *Nat. Energy* **2025**, *10*, 285–286.

[4] Chen, Z.; Zhi, C. Y. Chalcogens for high-energy batteries. *Nat. Rev. Mater.* **2025**, *10*, 268–284.

[5] Aniskevich, Y.; Myung, S. T. Gains and losses in zinc-ion batteries by proton- and water-assisted reactions. *Chem. Soc. Rev.* **2025**, *54*, 4531–4566.

[6] Xu, H. Y.; Geng, P. B.; Feng, W. C.; Du, M.; Kang, D. J.; Pang, H. Recent advances in metal–organic frameworks for electrochemical performance of batteries. *Nano Res.* **2024**, *17*, 3472–3492.

[7] Li, Y. T.; Zhao, C. R.; Xu, Y. F.; Liu, Z. Y.; Li, M.; Huang, Q.; Wu, X. High capacity and temperature adaptive aqueous zinc ion batteries through Ca^{2+} intercalated into $NH_4V_4O_{10}$ cathode materials. *Nano Research Energy* **2025**, *4*, e9120173

[8] Gao, H. Y.; Xie, J. F.; Zhang, S. R.; Mei, C. J.; Liu, J.; Du, H. Q.; Zhao, C. S.; Ni, W. H.; Huang, H.; Xue, Q. Non-metal anion doping construction of the durable cathode with optimized oxygen vacancies in aqueous zinc-ion batteries. *Nano Research Energy* **2025**, *4*, e9120182

[9] Chen, A.; Li, D. D.; Li, Q.; Chen, Z.; Huang, Z. D.; Zhi, C. Y. Cathode materials for zinc-based batteries. *Nano Research Energy* **2025**, *4*, e9120204

[10] Li, K. X.; Li, R.; Guan, T. T.; Wang, L.; Xie, L. L.; Han, Q.; Qiu, X. J.; Cao, X. Y.; Zhu, L. M. Recent advancements in cation-intercalated vanadium oxide cathode materials for zinc-ion batteries. *Chem. Eng. J.* **2025**, *507*, 159891.

[11] Lu, B. J.; Deng, J. Q.; Wu, Z. N.; Yu, H. X.; Yan, L.; Zhang, L. Y.; Yi, T. F.; Shu, J. Aqueous zinc–sulfur batteries: From challenges to strategies. *Adv. Mater.* **2025**, *37*, 2505203.

[12] Zhao, Y. W.; Zhu, J. X.; Li, C.; Zhang, S. C.; Zhang, R.; Li, P.; Hong, H.; Nian, Q. S.; Lyu, H. M.; Zhi, C. Y. Sulfur-based cathodes for aqueous zinc ion batteries. *J. Mater. Chem. C* **2024**, *12*, 14809–14815.

[13] Mehta, S.; Singh, M.; Garg, K.; Mishra, R. N.; Kumar, K.; Moirangthem, M.; Meena, S. K.; Nagaiah, T. C. Unlocking long life aqueous zinc–sulfur rechargeable battery derived from zinc waste powering 30 LEDs. *Adv. Energy Mater.* **2025**, *15*, 2501214.

[14] Thomas, T. S.; Sinha, A. P.; Mandal, D. Achieving high capacity and long cycling life in aqueous zinc–sulfur batteries with improved kinetics through electrolyte solvation engineering. *EES Batteries* **2025**, *1*, 609–619.

[15] Amiri, A.; Sellers, R.; Naraghi, M.; Polycarpou, A. A. Multifunctional quasi-solid-state zinc–sulfur battery. *ACS Nano* **2023**, *17*, 1217–1228.

[16] Zhao, X. Q.; Li, J.; Wang, S.; Sun, X. H.; Huo, M. D.; Zhao, Y. J.; Liu, H. Y.; Zheng, C. M. Constructing the multidirectional electrocatalytic restriction network for high-performance zinc–sulfur batteries. *Chem. Eng. J.* **2025**, *514*, 163224.

[17] Shen, S. Q.; Yuan, C.; Xu, Y.; Xie, Y. W.; Wang, L.; Yan, T. R.; Chen, S. Y.; Wang, L. Y.; Liu, T. F.; Zhang, L. Improving ZnS oxidation kinetics through nucleophilic regulation for high-performance zinc–sulfur batteries. *Adv. Funct. Mater.* **2025**, *35*, 2420258.

[18] Liu, J. H.; Wu, H.; Ye, C.; Qiao, S. Z. High-entropy sulfides catalyze rate-determining redox in fast-charging aqueous zinc–sulfur batteries. *Angew. Chem., Int. Ed.* **2025**, *64*, e202503472.

[19] Jiang, Y. X.; Sun, B. X.; Wang, D.; Yan, Y.; Shakouri, M.; Chen, H. Y.; Zhang, W.; Zhu, R. M.; Pang, H. Nanoreactor-driven uniform nano ZnS deposition in tunable porous carbon spheres for high-performance Zn–S batteries. *Adv. Sci.* **2025**, *12*, 2505218.

[20] Zhang, Q. H.; Zhang, W. L.; Wang, H.; Xu, C. H.; Li, R.; Xu, L.; Wang, X. Y.; Bian, J. H.; Wang, J. W.; Fu, F. Highly conductive sulfur iodide cathode accelerating sulfur redox kinetics for aqueous Zn–S batteries. *Nano Res.* **2026**, *19*, 94908050.

[21] Chen, Y. Y.; Ning, J. Y.; Wen, Y. X.; Yao, K. X.; Zhang, Y. X. Optimization strategies for high-performance aqueous zinc–sulfur batteries: Challenges and future perspectives. *Energy Mater.* **2025**, *5*, 500035.

[22] Thomas, T. S.; Sinha, A. P.; Mandal, D. Modulating electrolyte solvation for high-performance aqueous zinc–sulfur batteries. *J. Mater. Chem. A* **2024**, *12*, 21350–21356.

[23] Zhao, Z. X.; Tian, L. L.; Bai, Q.; Pathak, R.; Chen, J. J.; Ye, Y. C.; Wang, Y. Z.; Elam, J. W.; Wang, X. M. Dual-functional organoiodide additive for highly efficient sulfur redox kinetics and zinc regulation in aqueous zinc–sulfur Batteries. *Adv. Funct. Mater.* **2025**, *35*, 2501332.

[24] Wang, Z. S.; Yang, X. Y.; Wei, Y. J.; Wang, D. W. *In-situ* generated sulfur/porous carbon nanocomposites featuring enhanced specific surface area for aqueous zinc–sulfur batteries with small electrochemical polarization. *J. Power Sources* **2025**, *627*, 235829.

[25] Ge, Z. Q.; Liu, H. N.; Wang, S.; Ma, Y. J.; Xu, W. H.; Su, L. H.; Han, L.; Gong, L. Y.; Wang, J. Optimizing aqueous zinc–sulfur battery performance via regulating acetonitrile co-solvents and carbon nanotube carriers. *ChemSusChem* **2025**, *18*, e202401429.

[26] Zhang, Y.; Amardeep, A.; Wu, Z. R.; Tao, L.; Xu, J.; Freschi, D. J.; Liu, J. A tellurium-boosted high-areal-capacity zinc–sulfur battery. *Adv. Sci.* **2024**, *11*, 2308580.

[27] Wanyan, B.; Zhan, Y. Y.; Miao, Z. H.; Guo, W. B.; Wang, J. H.; Yan, L.; Zhang, L. Y.; Yu, H. X.; Yi, T. F.; Shu, J. Energetic aqueous zinc–sulfur battery achieved via co-solvent and redox mediator synergistic regulation. *Compos. Part B: Eng.* **2024**, *284*, 111709.

[28] Hei, P.; Sai, Y.; Liu, C.; Li, W. J.; Wang, J.; Sun, X. Q.; Song, Y.; Liu, X. X. Facilitating the electrochemical oxidation of ZnS through iodide catalysis for aqueous zinc–sulfur batteries. *Angew. Chem., Int. Ed.* **2024**, *63*, e202316082.

[29] Li, J. B.; Cong, J. L.; Ren, Y. B.; Ji, H. J.; Li, Z.; Huang, Y. H. Constructing a raincoat-like protective layer on sulfur cathode for aqueous Zn–S batteries. *Energy Storage Mater.* **2024**, *70*, 103541.

[30] Hao, J. N.; Zhang, S. J.; Wu, H.; Yuan, L. B.; Davey, K.; Qiao, S. Z. Advanced cathodes for aqueous Zn batteries beyond Zn^{2+} intercalation. *Chem. Soc. Rev.* **2024**, *53*, 4312–4332.

[31] Guo, Y. Q.; Lim, G. J. H.; Verma, V.; Cai, Y.; Chan, K. K.; Tang, E. J. J.; Srinivasan, M. Recent progress in zinc sulfur batteries: Mechanism, challenges, and perspectives. *Chem. Eng. J.* **2024**, *498*, 155329.

[32] Chen, L. T.; Liu, X. Q.; Tang, Y. C.; Wen, Z. P.; Li, C. C. Recent advancement in electrolyte optimization for rechargeable aqueous zinc–sulfur (Zn–S) batteries. *Curr. Opin. Electrochem.* **2024**, *47*, 101555.

[33] Wu, W. L.; Wang, S. B.; Lin, L.; Shi, H. Y.; Sun, X. Q. A dual-mediator for a sulfur cathode approaching theoretical capacity with low overpotential in aqueous Zn–S batteries. *Energy Environ. Sci.* **2023**, *16*, 4326–4333.

[34] Patel, D.; Sharma, A. K. Minireview on aqueous zinc–sulfur batteries: Recent advances and future perspectives. *Energy Fuels* **2023**, *37*, 10897–10914.

[35] Zhang, W. W.; Wang, M. L.; Ma, J. K.; Zhang, H.; Fu, L.; Song, B.; Lu, S. T.; Lu, K. Bidirectional atomic iron catalysis of sulfur redox conversion in high-energy flexible Zn–S battery. *Adv. Funct. Mater.* **2023**, *33*, 2210899.

[36] Zhao, S. F.; Wu, X. S.; Zhang, J. L.; Li, C. J.; Cui, Z. X.; Hu, W. H.; Ma, R. G.; Li, C. M. Biomass-derived porous carbon with single-atomic cobalt toward high-performance aqueous zinc–sulfur batteries at room temperature. *J. Energy Chem.* **2024**, *95*, 325–335.

[37] Dai, P. H.; Lang, J.; Huang, W. Y.; Ma, L.; Zhao, X. R.; Lin, X. J.; Li,

Q.; Li, H. P.; Liu, T. C.; Amine, K. et al. Spin state modulation via magnetic fields in Fe single-atom catalysts for high-performance aqueous zinc–sulfur batteries. *ACS Nano* **2025**, *19*, 21083–21094.

[38] Song, M.; Zhang, Q.; Luo, G. Y.; Hu, H. Y.; Wang, D. L. Coordination structure engineering of single atoms derived from MOFs for Electrocatalysis. *Coord. Chem. Rev.* **2025**, *523*, 216281.

[39] Chai, Y. C.; Wei, F. F.; Cao, L. R.; Wang, X. D.; Lin, S.; Lin, J.; Zhang, T. Peripheral effect promotes single-atom catalysis. *Coord. Chem. Rev.* **2025**, *536*, 216649.

[40] Dong, C. X.; Ma, C. N.; Zhou, C.; Yu, Y. K.; Wang, J. J.; Yu, K. S.; Shen, C. L.; Gu, J. P.; Yan, K. J.; Zheng, A. Q. et al. Engineering d–p orbital hybridization with P, S co-coordination asymmetric configuration of single atoms toward high-rate and long-cycling lithium–sulfur battery. *Adv. Mater.* **2024**, *36*, 2407070.

[41] Wang, Q. C.; Lyu, L. L.; Hu, X.; Fan, W. Q.; Shang, C. Y.; Huang, Q. R.; Li, Z. P.; Zhou, Z.; Kang, Y. M. Tailoring the surface curvature of the supporting carbon to tune the d-band center of Fe–N–C single-atom catalysts for zinc–urea–air batteries. *Angew. Chem., Int. Ed.* **2025**, *64*, e202422920.

[42] Funke, H.; Scheinost, A. C.; Chukalina, M. Wavelet analysis of extended X-ray absorption fine structure data. *Phys. Rev. B* **2005**, *71*, 094110.

[43] Ravel, B.; Newville, M. *ATHENA, ARTEMIS, HEPHAESTUS*: Data analysis for X-ray absorption spectroscopy using *IFEFFIT*. *J. Synchrotron Radiat.* **2005**, *12*, 537–541.

[44] Funke, H.; Chukalina, M.; Scheinost, A. C. A new *FEFF*-based wavelet for EXAFS data analysis. *J. Synchrotron Radiat.* **2007**, *14*, 426–432.

[45] Cychosz, K. A.; Guillet-Nicolas, R.; García-Martínez, J.; Thommes, M. Recent advances in the textural characterization of hierarchically structured nanoporous materials. *Chem. Soc. Rev.* **2017**, *46*, 389–414.

[46] Ferrari, A. C.; Robertson, J. Raman spectroscopy of amorphous, nanostructured, diamond-like carbon, and nanodiamond. *Philos. Trans. A: Math. Phys. Eng. Sci.* **2004**, *362*, 2477–2512.

[47] Yin, Q. W.; Duan, Y. H.; Du, J. L.; Zhang, H. Z.; Fu, Q.; Yang, X. F.; Li, X. F. Potential-controlled pre-SEI regulation for improved lithium reversibility in anode-free solid-state lithium metal batteries. *Adv. Mater.* **2025**, *37*, 2502077.

[48] Chen, Z.; Huang, Z. D.; Zhu, J. X.; Li, D. D.; Chen, A.; Wei, Z. Q.; Wang, Y. Q.; Li, N.; Zhi, C. Y. Highly reversible positive-valence conversion of sulfur chemistry for high-voltage zinc–sulfur batteries. *Adv. Mater.* **2024**, *36*, 2402898.

[49] Li, J.; Liu, J. L.; Xie, F. X.; Bi, R.; Zhang, L. Synergistic electrocatalysis and spatial nanoconfinement to accelerate sulfur conversion kinetics in aqueous Zn–S battery. *Angew. Chem.* **2024**, *136*, e202406126.

[50] Chang, G.; Liu, J. L.; Hao, Y. S.; Huang, C.; Yang, Y. J.; Qian, Y.; Chen, X. H.; Tang, Q. L.; Hu, A. P. Bifunctional electrolyte additive with redox mediation and capacity contribution for sulfur cathode in aqueous Zn–S batteries. *Chem. Eng. J.* **2023**, *457*, 141083.

[51] Zhang, H.; Yang, M.; Xiao, J.; Wu, Z. B.; Xin, W. L.; Xiao, X. L.; Niu, M. F.; Yan, Z. C.; Zhu, Z. Q. Internal electron donor accelerated sulfur redox for aqueous Zn–S batteries. *Adv. Funct. Mater.* **2024**, *34*, 2406125.

[52] Guo, Y. F.; Zhu, X. Q.; Zhang, J.; Zhang, T.; Wang, Z. L.; Shan, M. H.; Wang, F.; Cao, C. C.; Xu, G. Y.; Zhu, M. F. Engineering electrolyte network structure for improved kinetics and dendrite suppression in Zn–S batteries. *Angew. Chem., Int. Ed.* **2025**, *64*, e202422047.

[53] Brezesinski, T.; Wang, J.; Tolbert, S. H.; Dunn, B. Ordered mesoporous α-MoO_3 with iso-oriented nanocrystalline walls for thin-film pseudocapacitors. *Nat. Mater.* **2010**, *9*, 146–151.

[54] Hei, P.; Sai, Y.; Yu, L.; Lin, Y. L.; Li, B.; Hu, G. X.; Wu, W. L.; Wang, J.; Sun, X. Q.; Liu, X. X. et al. Cosolvent electrolyte design for high-voltage aqueous zinc–sulfur batteries. *J. Am. Chem. Soc.* **2025**, *147*, 27802–27811.

[55] Zhang, H.; Shang, Z. T.; Luo, G.; Jiao, S. H.; Cao, R. G.; Chen, Q. W.; Lu, K. Redox catalysis promoted activation of sulfur redox chemistry for energy-dense flexible solid-state Zn–S battery. *ACS Nano* **2022**, *16*, 7344–7351.

[56] Wang, M. L.; Zhang, H.; Ding, T. H.; Wu, F. J.; Fu, L.; Song, B.; Cao, P. F.; Lu, K. Simultaneous acceleration of sulfur reduction and oxidation on bifunctional electrocatalytic electrodes for quasi-solid-state Zn–S batteries. *Sci. China Chem.* **2024**, *67*, 1531–1538.

[57] Wang, D. W.; Kong, X. Y.; Wang, Z. S.; Zhang, X. Y.; Zhang, J.; Chen, Y. H. Dual-functional Fe_3O_4-decorated porous carbon nanosheets for kinetics-enhanced aqueous zinc–iodine batteries. *Green Carbon* **2025**, *3*, 382–392.